Japanese Journal of Applied Physics

REGULAR PAPER

Accuracy verification in ultrasonic elasticity measurement within intima-media complex visible range using phantom experimental system

To cite this article: Seira Akiyama *et al* 2021 *Jpn. J. Appl. Phys.* **60** SDDA07

Japanese Journal of Applied Physics **60**, SDDA07 (2021) **REGULAR PAPER**
https://doi.org/**10.35848/1347-4065/abef0d**

Accuracy verification in ultrasonic elasticity measurement within intima-media complex visible range using phantom experimental system

Seira Akiyama[1], Shohei Mori[2*], Mototaka Arakawa[1,2], and Hiroshi Kanai[1,2]

[1]*Graduate School of Biomedical Engineering, Tohoku University, Sendai, Miyagi 980-8579, Japan*
[2]*Graduate School of Engineering, Tohoku University, Sendai, Miyagi 980-8579, Japan*

[*]E-mail: mori@ecei.tohoku.ac.jp

Received December 1, 2020; revised February 10, 2021; accepted March 16, 2021; published online April 7, 2021

Studies to investigate the ultrasound elasticity measurement of the carotid artery, for early detection of arteriosclerosis, are ongoing. In the long-axis cross-sectional measurement in vivo, the position where the intima-media complex (IMC) is visible on the B-mode image was assumed to be the central axis of the short-axis view of the carotid artery. However, the IMC is also visible near the central axis of the short-axis view of the carotid artery. In the present study, accuracy in elasticity measurement within the IMC visible range was evaluated through a phantom experiment. The elasticities of the posterior wall measured at plural points within the IMC visible range differed by up to 6%. From the experimental results, we concluded that for the highest accuracy, it is important to measure along the central axis of the short-axis view of the carotid artery.

1. Introduction

Cardiovascular diseases such as strokes and myocardial infarctions are the leading causes of death worldwide;[1] these diseases are caused primarily by arteriosclerosis. In the early stages of arteriosclerosis, the cholesterol content in the aorta affects the elasticity of the arterial wall; therefore, measuring the elasticity of the arterial wall can aid early detection of arteriosclerosis.[2]

Diagnostic methods for arteriosclerosis include angiography, angioscopy, intravascular ultrasound, and radiographic imaging.[3] As these diagnostic techniques are invasive, they are not suitable for non-invasively and repetitively diagnosing changes over time in the early stages of arteriosclerosis. Non-invasive methods for diagnosing arteriosclerosis include magnetic resonance imaging, intima-media complex (IMC) thickness (IMT) measurement using ultrasound,[4] and blood flow measurement using ultrasound. Because these diagnostic methods mainly measure information such as the shape of the arterial wall, the size of the atherosclerotic plaque, and the degree of stenosis, it is difficult to diagnose the histological characteristics.

Elasticity measurement is one of the approaches for evaluating the tissue characteristics of the arterial wall.[5–11] Non-invasive evaluation methods for determining the elastic properties of the arterial wall include pulse wave velocity measurement,[12,13] stiffness parameter measurement,[14,15] and flow-mediated dilation.[16] These methods can be used to evaluate the average elastic properties of the entire wall.

To measure the local elasticity of the arterial wall using ultrasound, the change in thickness of the arterial wall is measured in a local region, approximately 0.1 mm in the long-axis direction of the blood vessel.[17–21] This method can measure the distribution of local elasticities and evaluate the histological characteristics of heterogeneous atherosclerotic plaques. Kanai et al. developed the phased tracking method to measure the minute displacement of the arterial wall in one heartbeat.[22] The elasticity of the arterial wall can be estimated from the thickness change measured from the minute displacement of the arterial wall and the pulse pressure measured by a sphygmomanometer. Kanai et al. presented an elasticity tomographic image by measuring the local elasticity of the carotid artery.[23] Inagaki et al. developed a method for tissue characterization of the arterial wall by analyzing the elasticity distribution of the tissue illustrated by the elasticity tomographic image.[24]

As the true value of elasticity is unknown in vivo, the measurement accuracy cannot be verified in vivo. Therefore, the measurement accuracy of elasticity was verified through phantom experiments in a previous study. In vivo, elasticity was measured on the long-axis view of the carotid artery by assuming that the position where the IMC is visible corresponds to the central axis of the short axis of the carotid artery. Therefore, the elasticity of the phantom was also measured on the long-axis view in that study.[25] However, the position where the IMC can be seen is not always the central axis; the IMC can be observed in the vicinity of the central axis in the short-axis view of the carotid artery. Therefore, it is important to assess the accuracy of elasticity measurement within the IMC visible range. For this purpose, it is necessary to validate the elasticity measurement accuracy in the short-axis view, where the position of the central axis can be identified.

In our previous study,[26] we conducted a phantom experiment to evaluate the accuracy of ultrasound elasticity measurement on the central axis of the short-axis view. However, the elasticity measurement accuracy in positions neighboring the central axis has not been examined yet.

In the present study, the accuracy of elasticity measurement within the IMC visible range was verified. First, the RF signal measured on the central axis of the short-axis view was analyzed, and the elasticity was estimated. The elasticity was calculated using the external radius change, and the result was compared with that of the laser sensor measurement. Then, the elasticity calculated using the change in thickness was compared with that calculated using the external radius change in the ultrasound measurement. Finally, elasticity was measured at positions deviated from the central axis of the short axis of the phantom; it was then compared with the elasticity measured along the central axis.

2. Principles

2.1. Measurement of elasticity using thickness change (ultrasound)

The change in arterial wall thickness $\Delta h(t)$ that occurs with pulsation is measured by the phased tracking method.[22]

Assuming that the arterial wall is elastically incompressible[27] and isotropic and the artery is strongly restricted in the longitudinal direction (i.e. the strain in the longitudinal direction is negligible), the elastic modulus E_θ^h in the circumferential direction is expressed by Eq. (1) as follows:[28–30]

$$E_\theta^h = \frac{3}{8}\left(1 + \frac{2r_0}{h_0}\right)\frac{\Delta p}{-\frac{\Delta h}{h_0}}, \tag{1}$$

where h_0 is the initial thickness, r_0 is the initial arterial inner radius, and $\Delta p(t)$ is the incremental internal pressure. From the relationship between the incremental internal pressure $\Delta p(t)$ and the incremental strain $-\Delta h(t)/h_0$, the slope for one cycle of circulation $\Delta p/\{-\Delta h/h_0\}$ was estimated using the least-squares method to obtain E_θ^h. Thus, the term $\Delta p/\{-\Delta h/h_0\}$ on the right side of Eq. (1) becomes a time-independent constant. The initial thickness h_0, the initial arterial inner radius r_0, and the change in the arterial wall thickness $\Delta h(t)$ were measured through ultrasound.

2.2. Measurement of elasticity using external diameter change (laser and/or ultrasound)

Since the thickness change cannot be measured by a laser sensor, the elasticity was measured using the external diameter change. Assuming that the wall thickness is uniform in the circumferential direction, the incremental elasticity E_{inc} can be calculated using the external radius change $\Delta r_{\mathrm{e}}(t)$ of the phantom, as expressed by Eq. (2)[31]

$$E_{\mathrm{inc}} = \frac{3}{2}\frac{r_0^2}{r_{\mathrm{e}}^2 - r_0^2}\frac{\Delta p}{\frac{\Delta r_{\mathrm{e}}}{r_{\mathrm{e}}}}, \tag{2}$$

where r_{e} is the external radius before deformation. Equation (2) can also be derived from Eq. (1) by introducing the assumptions that the wall thickness is uniform in the circumferential direction, $\Delta r_{\mathrm{e}}(t)^2 \ll r_{\mathrm{e}}^2$, $\Delta r_0(t)^2 \ll r_0^2$, and $h_0^2 \ll (2r_0)^2$.

From the relationship between the incremental internal pressure $\Delta p(t)$ and the incremental strain $\Delta r_{\mathrm{e}}(t)/r_{\mathrm{e}}$, the slope for one cycle of circulation $\Delta p/\{\Delta r_{\mathrm{e}}/r_{\mathrm{e}}\}$ was estimated using the least-squares method to obtain E_{inc}. Therefore, the term $\Delta p/\{\Delta r_{\mathrm{e}}/r_{\mathrm{e}}\}$ on the right side of Eq. (2) becomes a time-independent constant. For measurement using the laser sensor, the initial arterial radius r_0 was calculated as the difference between the external radius r_{e} (before the deformation) measured by the laser sensor and the initial thickness h_0 measured by the ultrasound; the external radius change $\Delta r_{\mathrm{e}}(t)$ was measured by the laser sensor. To compare the result of the ultrasound with that of the laser sensor, E_{inc} was also estimated in the ultrasound measurement. In the ultrasound measurement, the initial arterial inner radius r_0, the external radius before the deformation r_{e}, and the external radius change $\Delta r_{\mathrm{e}}(t)$ were measured using ultrasound.

2.3. Sound velocity estimation in phantom

The initial thicknesses h_{ant} and h_{pos} of the anterior and posterior walls, respectively, the inner radius r_0, and the external radius r_{e} of the phantom in Eqs. (1) and (2) are expressed in terms of the sound velocity c_{p} of the phantom as follows:

$$h_{\mathrm{ant}} = c_{\mathrm{p}} t_{\mathrm{ant}}, \tag{3}$$

$$h_{\mathrm{pos}} = c_{\mathrm{p}} t_{\mathrm{pos}}, \tag{4}$$

$$r_0 = \frac{c_{\mathrm{w}} t_{\mathrm{lum}}}{2}, \tag{5}$$

$$r_{\mathrm{e}} = \frac{c_{\mathrm{w}} t_{\mathrm{lum}} + c_{\mathrm{p}}(t_{\mathrm{ant}} + t_{\mathrm{pos}})}{2}, \tag{6}$$

where c_{w} is the speed of sound in water and t_{ant}, t_{lum}, and t_{pos} are the propagation times of the ultrasound pulse in the anterior wall of the phantom, the phantom lumen, and the posterior wall of the phantom, respectively. In the present study, c_{w} was measured using water temperature.[32] From Eqs. (1)–(6), it is clear that knowledge of the sound velocity c_{p} of the phantom is necessary for elasticity measurement. This estimated sound velocity c_{p} was used for introducing the initial thickness h_0, the initial arterial inner radius r_0, and the change in the arterial wall thickness $\Delta h(t)$ in Eq. (1), and the initial arterial inner radius r_0, the external radius before deformation r_{e}, and the external radius change $\Delta r_{\mathrm{e}}(t)$ in Eq. (2). Therefore, the sound velocity of the phantom was estimated using the RF signal obtained from an acrylic block placed under the phantom in water.

Figure 1 illustrates (a) the schematic of the experiment for measuring the phantom sound velocity, (b) the schematic of the B-mode image obtained by using the experimental configuration in Fig. 1(a). In this condition, the ultrasound propagation times from the probe to the acrylic block at positions p_1 and p_2, depicted in Fig. 1(b), are different due to the difference in sound velocities of the water and the phantom. Therefore, the visualized depth of the acrylic block on the conventional B-mode image, which assumes a constant sound velocity, is changed by the lateral position, as depicted in Fig. 1(b). The sound velocity of the phantom can be measured by comparing the propagation times of the two ultrasound beams depicted by yellow lines, which are measured along with positions p_1 and p_2. The distance x_1 from the probe to the acrylic block at position p_1 and x_2 from the probe to the acrylic block at position p_2 are expressed by Eqs. (7) and (8), respectively

$$x_1 = c_{\mathrm{w}}(t_1 - t_{\mathrm{ant}} - t_{\mathrm{pos}}) + c_{\mathrm{p}}(t_{\mathrm{ant}} + t_{\mathrm{pos}}), \tag{7}$$

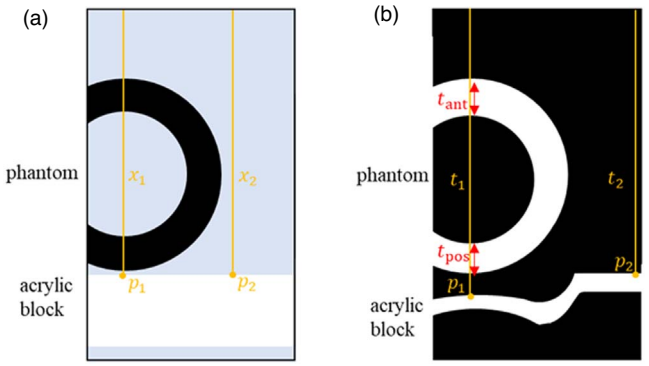

Fig. 1. (Color online) (a) Schematic for estimation of sound velocity c_{p} in phantom and (b) schematic of the B-mode image under experimental configuration in Fig. 1(a).

$$x_2 = c_w t_2, \tag{8}$$

where t_1 and t_2 are the propagation times of the ultrasound pulse from the probe to the acrylic block at positions p_1 and p_2, respectively. Because the distances x_1 and x_2 from the probe to the acrylic block are equal, as depicted in Fig. 1(a), the sound velocity c_p of the phantom can be calculated from Eqs. (7) and (8), as shown in Eq. (9)

$$c_p = c_w \left(1 - \frac{t_1 - t_2}{t_{ant} + t_{pos}} \right). \tag{9}$$

3. Experimental method

Figure 2 shows (a) the schematic of the experimental system and (b) the setting of the ultrasound probe and the laser sensor. Figure 2(b) is a side view of Fig. 2(a). The ultrasound measurement was conducted using an ultrasonic diagnostic device (SSD-6500, Aloka, Japan). A linear probe with a central frequency of 7.5 MHz was used. The values of the sampling frequency, beam spacing, and frame rate were 40 MHz, 150 μm, and 286 Hz, respectively.

Figure 3 shows a schematic of the laser sensor measurement. The laser displacement meter (IG-028, KEYENCE, Japan) used in the study, which is composed of a light transmitter and a light receiver, can measure the length of the area where laser light is blocked, that is, the external diameter of the phantom.

A black silicone tube (Shonan Kasei, Japan) with an ASKER-C hardness of 10°, an external diameter of 9 mm, an inner diameter of 7 mm, and a wall thickness of 1 mm (nominal value) was used as a simulated carotid artery phantom. Carbon powders with 5 wt% were included as scatters in the tube. In the estimations of elasticity using Eqs. (1) and (2), these nominal values were not used, as described in Sects. 2.1 and 2.2. The ASKER-C hardness was measured by a durometer (ASKER-C) specified by the Society of Rubber Science and Technology in Japan. A pulsatile pump unit (EC-8, Fuyo, Japan) was used to simulate the in vivo condition of blood circulation. The number of pulsations was set to 60 times min^{-1}. The water in the aquarium was degassed and purified; for circulation, tap water was used.

The pressure sensor (PS-1KC, Kyowa, Japan) was used to measure the incremental internal pressure $\Delta p(t)$, which is used in Eqs. (1) and (2). Because the time delay of the waveforms measured by the pressure sensors [presented in Fig. 2(a) as (i) and (ii)] was sufficiently small, the pressure measured by sensor (i) was used to calculate the elasticity.

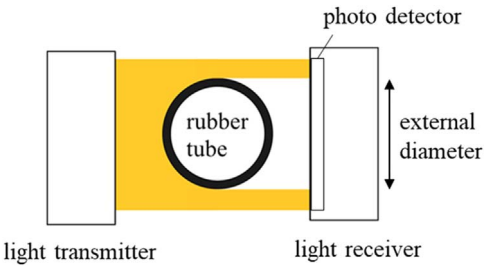

Fig. 3. (Color online) Schematic of laser sensor measurement.

In a previous study,[26] the phantom was placed in air for the laser sensor measurement because the measurement was unstable when the phantom was placed in tap water; this instability was due to the scattering of the laser by dust and air bubbles in tap water. Because the ultrasound measurement could not be conducted in the air, the measurement conditions were different between the laser sensor and ultrasound measurements, and the measured waveforms of external diameter change did not correspond for the two measurements. In the present study, the laser sensor measurement in water was stabilized using degassed and purified water in the water tank wherein the phantom was placed. Therefore, the measurements could be conducted under the same conditions using the ultrasound and the laser sensor, and the simultaneous measurement was realized. A sheet-shaped laser beam was used to visually align the ultrasound beam with the laser beam.

4. Results and discussion

4.1. Sound velocity estimation in phantom

Figure 4 shows the envelopes of the RF signals measured on the ultrasound beams at positions p_1 and p_2 depicted in Fig. 1. The propagation times t_1 and t_2 of the ultrasound pulses from the ultrasound probe to the acrylic block at positions p_1 and p_2 , respectively, and the propagation times t_{ant} and t_{pos} in the anterior and posterior walls of the phantom, respectively, were measured from the peaks of the RF signal envelopes. Then, the sound velocity c_p of the phantom was estimated as 1066 m s^{-1} using Eq. (9).

4.2. Accuracy verification of elasticity measurement on central axis of short-axis view of phantom

Figure 5 shows (a) the B-mode image of the phantom in the short-axis view, (b) the M-mode image on the central axis of

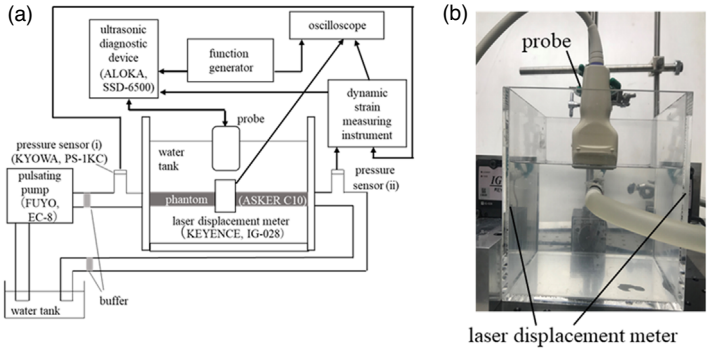

Fig. 2. (Color online) (a) Schematic of experimental system and (b) setting of the ultrasound probe and laser sensor.

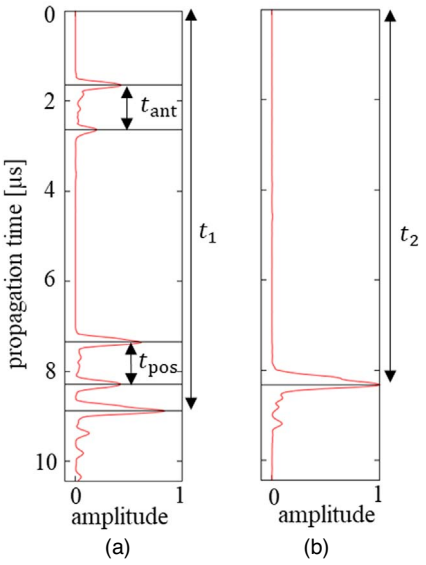

Fig. 4. (Color online) Envelope of RF signal at positions of two ultrasound beams, p_1 and p_2 (Fig. 1) used for estimating the sound velocity c_p in phantom.

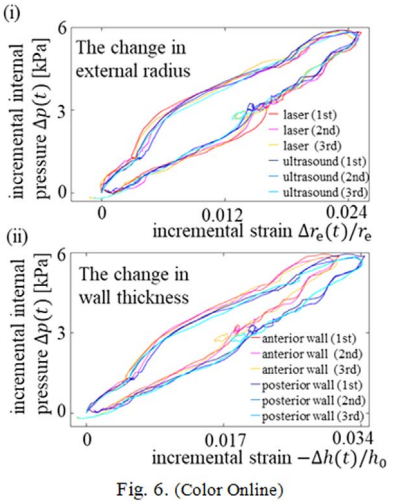

Fig. 6. (Color Online)

Fig. 6. (Color online) (i) Incremental internal pressure $\Delta p(t)$ and incremental strain $-\Delta h(t)/h_0$ of anterior and posterior walls measured by ultrasound and (ii) incremental internal pressure $\Delta p(t)$ and strain $\Delta r_e(t)/r_e$ measured by ultrasound or laser. Results for three cycles of pulsation are shown.

the phantom, (c)(i) the incremental internal pressure $\Delta p(t)$ measured by the pressure sensor and the incremental strain $\Delta r_e(t)/r_e$ measured by the laser sensor or ultrasound, and (c)(ii) the incremental internal pressure $\Delta p(t)$ measured by the pressure sensor and the incremental strain $-\Delta h(t)/h_0$ measured by the ultrasound. Each result presented in Figs. 5(b) and 5(c) was measured along the central axis of the short-axis view of the phantom [red line in Fig. 5(a)]. From Fig. 5(c)(i), the changes in the external radius $\Delta r_e(t)$ correspond well in the ultrasound and laser sensor measurements. As depicted in Fig. 5(c)(ii), the thickness changes $\Delta h(t)$ of the anterior and posterior walls are not congruent in the ultrasound measurement.

Figure 6(i) depicts the relationship between the incremental internal pressure $\Delta p(t)$ measured by the pressure sensor and the incremental strain $\Delta r_e(t)/r_e$ measured by the ultrasound or laser sensor. Figure 6(ii) depicts the relationship between the incremental internal pressure $\Delta p(t)$ measured by the pressure sensor and the incremental strain $-\Delta h(t)/h_0$, measured by the ultrasound. The measurement results for three cycles of pulsation are shown in Fig. 6. In Fig. 6(ii), the measured hysteresis curves correspond well with the three measurements for the anterior or posterior walls. However, the hysteresis curves of the anterior and posterior walls are not congruent because the incremental strain $-\Delta h(t)/h_0$ is different for the anterior and posterior walls, as shown in Fig. 5(c)(ii).

To investigate the disagreement between the incremental strains $-\Delta h(t)/h_0$ of the anterior and posterior walls of the phantom, the phantom was rotated 180° concerning the center of the short-axis view, and the incremental strains $-\Delta h(t)/h_0$ were measured using the ultrasound. Figure 7 depicts the internal pressure $\Delta p(t)$ and the incremental strain $-\Delta h(t)/h_0$. Figure 7(a) depicts the incremental strain $-\Delta h(t)/h_0$ at position A (anterior wall) and position B (posterior wall). Figure 7(b) depicts the same parameters as

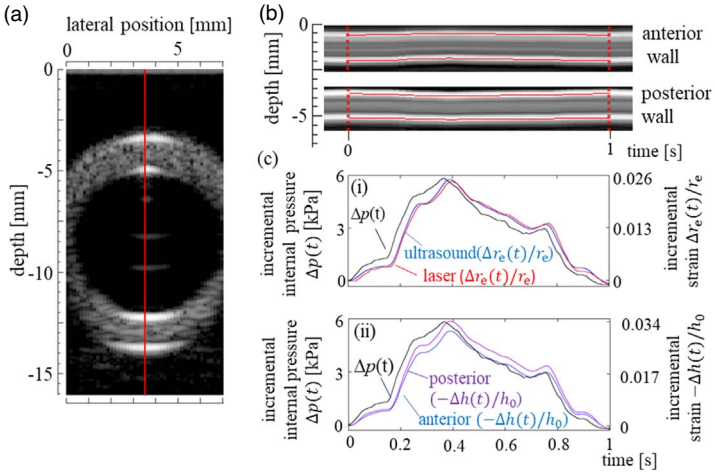

Fig. 5. (Color online) (a) B-mode image of short-axis cross-sectional view of the phantom, (b) M-mode image on the red line in Fig. 5(a), (c)(i) incremental internal pressure $\Delta p(t)$ and incremental strain $\Delta r_e(t)/r_e$ measured by ultrasound and laser sensor, and (c)(ii) incremental internal pressure $\Delta p(t)$ and incremental strain $\Delta h(t)/h_0$ on anterior and posterior walls measured by ultrasound. Figures 5(b) and 5(c) depict the measurement results on the central axis of the short-axis view of the phantom and results for the first cycle measurement of pulsation.

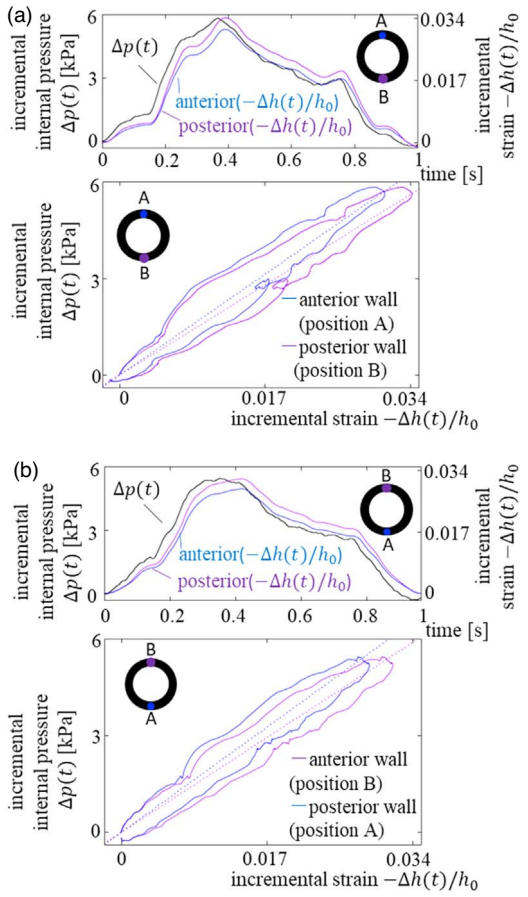

Fig. 7. (Color online) (a) Incremental internal pressure $\Delta p(t)$ and incremental strain $-\Delta h(t)/h_0$ where point A is the anterior wall and point B is the posterior wall and (b) incremental internal pressure $\Delta p(t)$ and incremental strain $-\Delta h(t)/h_0$ where point B is the anterior wall and point A is the posterior wall.

Fig. 7(a) after the phantom was rotated 180° from the condition in Fig. 7(a).

Let us discuss the difference in the results at positions A and B. The differences in incremental strains for positions A and B might be due to unequal sound velocity distribution caused by the inhomogeneity of the carbon used in the present study. However, it is difficult to separately measure the sound velocities in the anterior and posterior walls in the phantom because only the average sound velocity of the anterior and posterior walls can be computed using Eq. (9). The wall thickness might also be unevenly distributed. Even if the wall thickness is uneven in the circumferential direction, this difference does not affect the estimation of elasticity because Eq. (1) does not require the assumption of uniformity of the wall thickness in the circumferential direction and considers the locality of the initial wall thickness. Thus, we concluded that the difference in the hysteresis loop between positions A and B was caused by the difference in the actual elasticity and/or sound velocity at positions A and B of the phantom. The locality of the actual elasticity and the sound velocity of the phantom in the circumferential direction will be examined in future studies.

Table I presents the elasticities E_{inc} calculated using the changes in external radius $\Delta r_{\mathrm{e}}(t)$ measured by the laser sensor and ultrasound; it also shows the elasticities E_{θ}^{h} of the anterior and posterior walls calculated using the thickness change $\Delta h(t)$ measured by the ultrasound. The elasticities were measured for three different cycles of pulsation, and the average and standard deviation are shown in Table I.

The elasticities E_{inc}, measured using the external radius changes $\Delta r_{\mathrm{e}}(t)$ for the laser sensor and ultrasound measurements, agreed within 0.8%. This confirmed that the accuracy of ultrasound elasticity measurement is similar to that of laser sensor measurement when the ultrasound elasticity measurement is conducted along the central axis of the short-axis view of the phantom.

In the ultrasound measurement, the elasticity E_{inc}, measured using the external radius change $\Delta r_{\mathrm{e}}(t)$, and the average of the elasticities E_{θ}^{h}, measured using the thickness changes $\Delta h(t)$ for the anterior and posterior walls, were within 0.05% of each other. Therefore, the elasticity E_{inc}, measured using the external radius change, represents the average of the elasticities of the anterior and posterior walls. The difference in elasticities E_{θ}^{h}, calculated from the thickness change $\Delta h(t)$ on the anterior and posterior walls, may reflect the inhomogeneity of elasticity and/or the inhomogeneity of sound velocity in the phantom, as discussed in Fig. 7. Thus, one advantage of ultrasound measurement over laser sensor measurement is that it can measure the local elasticity.

4.3. Effect of measurement position within IMC visible range

We examined the effect of deviation of the measurement position from the central axis of the short-axis view of the phantom on the elasticity measurement. Figure 8 shows (a) the B-mode image, (b) the maximum amplitude of the envelope of the RF signals obtained from the intima of the posterior wall, and (c) the elasticities of the posterior wall at plural positions in the lateral direction from the central axis of the short axis of the phantom. The blue line in Fig. 8(b) shows the range of −6 dB bandwidth where the maximum envelope amplitude of the posterior wall was 0 dB. Figure 8(c) depicts the elasticities estimated in three measurements with different cycles of pulsation.

When the measurement position was outside of the −6 dB bandwidth (i.e. outside of the enclosed region with blue lines), the elasticities decreased drastically. The reason for this elasticity measurement error outside the IMC visible range, depicted in Fig. 8(c), must be examined in future studies. For positions within the −6 dB bandwidth of the envelope amplitude from the intima of the phantom (i.e. inside the enclosed region with blue lines), the average values

Table I. Elasticity E_{inc} calculated using the change in external radius $\Delta r_{\mathrm{e}}(t)$ (laser, ultrasound) and elasticity E_{θ}^{h} calculated using thickness change $\Delta h(t)$ (anterior wall, posterior wall).

		E_{θ}^{h} [kPa] (ultrasound)		
E_{inc} [kPa] (laser)	E_{inc} [kPa] (ultrasound)	Anterior wall	Posterior wall	Average of anterior and posterior walls
507 ± 9	511 ± 3	535 ± 5	488 ± 5	512 ± 4

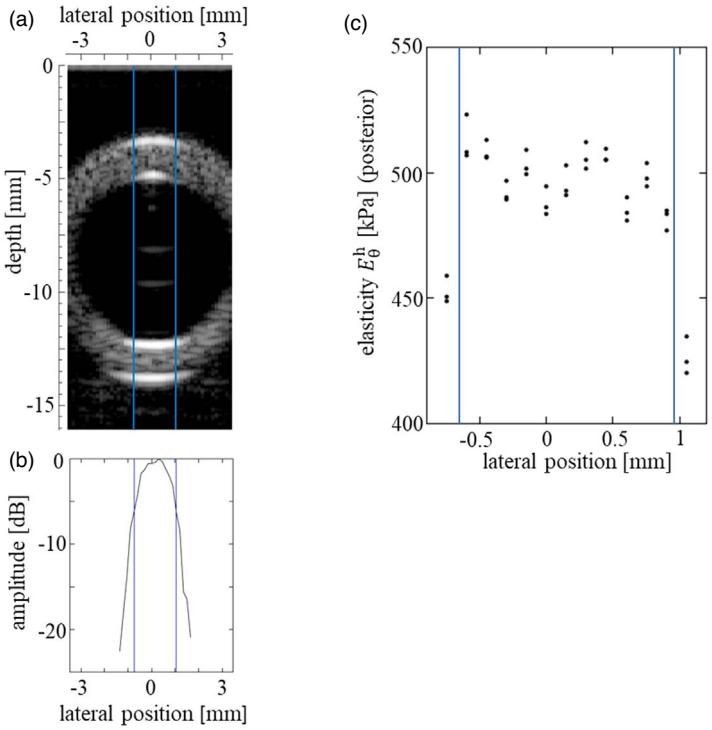

Fig. 8. (Color online) (a) B-mode image of short-axis cross-sectional view of the phantom, (b) envelope amplitude of intima of the posterior wall, and (c) elasticity of posterior wall measured on neighboring positions of the central axis of short-axis of the phantom.

of the posterior wall elasticity coincided within 6%. The region enclosed by blue lines in Fig. 8 (i.e. −6 dB bandwidth of the envelope amplitude from the intima) approximately corresponds to the IMC visible range in the in vivo measurement. Therefore, the results presented in Fig. 8(c) indicate that the elasticity of the posterior wall of the carotid artery can be measured with approximately 6% accuracy, if the condition for the IMC visible range in the phantom experiment of the present study is upheld in the in vivo measurement (i.e. if the IMC is visible within 9° from the central axis in vivo). The causes of differences in estimated elasticity within the IMC visible range may include the influence of refraction and the fact that the ultrasound measures the projection component of h_0, $\Delta h(t)$, and r_0 when measuring on the neighboring position of the central axis. In the short-axis measurement, these effects can be examined quantitatively because distance from the central axis can be measured. However, in the long-axis measurement, it is not possible to determine the distance from the central axis. Therefore, we concluded that for accurate elasticity measurement, it is important to measure the elasticity along the central axis of the carotid artery in the short-axis view.

5. Conclusions

In the present study, the accuracy of elasticity measurement was assessed through phantom experiments using ultrasound. First, sound velocity c_p of the phantom used for the elasticity measurement was estimated. Next, the elasticity of the phantom was measured using the sound velocity c_p of the phantom, and the accuracy of the ultrasound elasticity measurement along the central axis of the short-axis view of the phantom was verified. The elasticities E_{inc} calculated using the external radius changes $\Delta r_e(t)$, determined using ultrasound and laser sensor measurements, agreed within 0.8%. The elasticity E_{inc}, calculated using the external radius change $\Delta r_e(t)$, and the average of the elasticities E_θ^h of the anterior and posterior walls, calculated using the thickness changes $\Delta h(t)$, coincided within 0.05%. Finally, the elasticity was measured at positions deviated from the central axis of the short-axis view of the phantom. At positions corresponding to the IMC visible range in the in vivo measurement, the average values of the elasticity on the posterior wall differed by up to 6%. We concluded that for accuracy, it is important to measure the elasticity along the central axis of the carotid artery in the short-axis view.

In the future, we will examine an elasticity measurement method that considers the refraction and projection components for measurements within the IMC visible range. Moreover, the only guarantee for the stiffness of the phantom used in the present study was ASKER-C hardness; therefore, the accuracy of elasticity measurement was validated by comparing the results of a laser sensor and ultrasound measurements. Therefore, in future studies, Young's modulus of the phantom must be determined through mechanical testing and compared with the ultrasound measurement results.

Acknowledgments

This work was supported in part by JSPS KAKENHI 19KK0100.

1) K. J. Foreman et al., Lancet **392**, 2052 (2018).
2) T. I. Pynadath and D. P. Mukherjee, Atherosclerosis **26**, 311 (1977).
3) Y. Masuda, S. Naito, Y. Aoyagi, Z. Yamada, T. Uda, N. Morooka, S. Watanabe, and Y. Inagaki, Angiology **41**, 1037 (1990).
4) T. Yamagishi, M. Kato, Y. Koiwa, H. Hasegawa, and H. Kanai, J. Atherosclerosis Thrombosis **16**, 782 (2009).

5) D. S. Celermajer, K. E. Sorensen, V. M. Gooch, D. J. Spiegelhalter, O. I. Miller, I. D. Sullivan, K. Lloyd, and J. E. Deanfield, Lancet **340**, 1111 (1992).
6) J. Persson, J. Formgren, B. Israelsson, and G. Berglund, Arterioscler Thromb Vasc. Biol. **14**, 261 (1994).
7) K. Ikeshita, H. Hasegawa, and H. Kanai, Jpn. J. Appl. Phys. **47**, 4165 (2008).
8) K. Ikeshita, H. Hasegawa, and H. Kanai, Jpn. J. Appl. Phys. **48**, 07GJ10 (2009).
9) K. Ikeshita, H. Hasegawa, and H. Kanai, Jpn. J. Appl. Phys. **50**, 07HF08 (2011).
10) K. Ikeshita, H. Hasegawa, and H. Kanai, Jpn. J. Appl. Phys. **51**, 07GF14 (2012).
11) N. Ibrahim, H. Hasegawa, and H. Kanai, Jpn. J. Appl. Phys. **52**, 07HF03 (2013).
12) T. Nishiya, S. Senda, K. Katakura, M. Sugawara, M. Yuba, H. Morita, H. Masugata, K. Yoshikawa, H. Yokoi, and H. Matsuo, Jpn. J. Med. Ultrason. **22**, 695 (1995) [in Japanese].
13) D. A. McDonald, *Blood Flow in Arteries* (Edward Arnold Publishers, London, 1974) 2nd ed., p. 284.
14) K. Hayashi, H. Handa, S. Nagasawa, A. Okumura, and K. Moritake, J. Biomech. **13**, 175 (1980).
15) K. Moritake, H. Handa, A. Okumura, K. Hayashi, and H. Niimi, Neurol. Medico-Chir. **14pt1**, 47 (1974).
16) T. Saito, S. Mori, M. Arakawa, S. Ohba, K. Kobayashi, and H. Kanai, Jpn. J. Appl. Phys. **59**, SKKE04 (2020).
17) M. A. Hajdu, D. D. Heistad, J. E. Siems, and G. L. Baumbach, Circ. Res. **66**, 1747 (1990).
18) D. J. Mozersky, D. S. Sumnfr, D. E. Hokanson, and D. E. Strandness Jr., Circulation **46**, 948 (1972).
19) A. P. G. Hoeks, C. J. Ruissen, P. Hick, and R. S. Reneman, Ultrasound Med. Biol. **11**, 51 (1985).
20) H. Kanai, H. Hasegawa, N. Chubachi, Y. Koiwa, and M. Tanaka, IEEE Trans. Ultrason. Ferroelectr. Freq. Control **44**, 752 (1997).
21) H. Hasegawa, H. Kanai, N. Hoshimiya, N. Chubachi, and Y. Koiwa, Jpn. J. Appl. Phys. **37**, 3101 (1998).
22) H. Kanai, M. Sato, Y. Koiwa, and N. Chubachi, IEEE Trans. Ultrason. Ferroelectr. Freq. Control **43**, 791 (1996).
23) H. Kanai, H. Hasegawa, M. Ichiki, F. Tezuka, and Y. Koiwa, Circulation **107**, 3018 (2003).
24) J. Inagaki, H. Hasegawa, H. Kanai, M. Ichiki, and F. Tezuka, Jpn. J. Appl. Phys. **44**, 4593 (2005).
25) H. Hasegawa and H. Kanai, Jpn. J. Appl. Phys. **44**, 4609 (2005).
26) S. Akiyama, S. Mori, M. Arakawa, and H. Kanai, Proc. Symp. Ultrason. Electr. **41**, 1Pb1-2 (2020).
27) T. E. Carew, R. N. Vaishnav, and D. J. Patel, Circ. Res. **23**, 61 (1968).
28) D. J. Patel, J. S. Janicki, R. N. Vaishnav, and J. T. Young, Circ. Res. **32**, 93 (1973).
29) H. Hasegawa and H. Kanai, Proc. 2007 IEEE Int. Ultrasonics Symp., 2007, p. 860.
30) Y. Miyachi, M. Arakawa, and H. Kanai, Jpn. J. Appl. Phys. **57**, 07LF08 (2018).
31) D. H. Bergel, J. Physiol. **156**, 445 (1961).
32) W. Kroebel and K.-H. Mahrt, Acta Acustica United Acustica **35**, 154 (1976).